Critical properties of metallic and deconfined quantum phase transitions in Dirac systems

Zi Hong Liu [1], Matthias Vojta [1], Fakher F. Assaad,[2] and Lukas Janssen [1]

[1]*Institut für Theoretische Physik and Würzburg-Dresden Cluster of Excellence ct.qmat,*
Technische Universität Dresden, 01062 Dresden, Germany

[2]*Institut für Theoretische Physik und Astrophysik and Würzburg-Dresden Cluster of Excellence ct.qmat,*
Universität Würzburg, 97074 Würzburg, Germany

We characterize, by means of large-scale fermion quantum Monte Carlo simulations, metallic and deconfined quantum phase transitions in a bilayer honeycomb model in terms of their quantum critical and finite-temperature properties. The model features three distinct phases at zero temperature as a function of interaction strength. At weak interaction, a fully symmetric Dirac semimetal state is realized. At intermediate and strong interaction, respectively, two long-range-ordered phases, each breaking different symmetries are stabilized. The ordered phases feature partial and full gap openings in the fermion spectrum, respectively. We clarify the symmetries of the different zero-temperature phases and the symmetry-breaking patterns across the two quantum phase transitions between them. The first transition between the disordered and long-range-ordered semimetallic phases has previously been argued to be described by the $(2 + 1)$-dimensional Gross-Neveu-SO(3) field theory. By performing simulations with an improved symmetric Trotter decomposition, we further substantiate this claim by computing the critical exponents $1/\nu$, η_ϕ, and η_ψ, which turn out to be consistent with the field-theoretical expectation within numerical and analytical uncertainties. The second transition between the two long-range-ordered phases has previously been proposed as a possible instance of a metallic deconfined quantum critical point. We further develop this scenario by analyzing the spectral functions in the single-particle, particle-hole, and particle-particle channels. Our results indicate gapless excitations with a unique velocity, supporting the emergence of Lorentz symmetry at criticality. We also compute the finite-temperature phase boundaries of the ordered states above the fully gapped state at large interaction. The phase boundary vanishes smoothly in the vicinity of the putative metallic deconfined quantum critical point, in agreement with the expectation for a continuous or weakly first-order transition.

I. INTRODUCTION

Quantum critical points refer to continuous phase transitions occurring at absolute zero temperature. In two-dimensional systems consisting of only few atomically thin layers, a number of control parameters that may potentially drive such transitions exist, such as uniaxial or hydrostatic pressure, lattice mismatch, or twisting angle. In insulators, conventional quantum critical points are characterized by fluctuations of a bosonic order parameter alone. These quantum critical points can usually be fully understood in terms of a corresponding higher-dimensional classical transition within the Landau-Ginzburg-Wilson paradigm. In metals, by contrast, the presence of gapless fermionic degrees of freedom at the transition inhibits such a quantum-to-classical mapping. As potential platforms for physics beyond the Landau-Ginzburg-Wilson paradigm, metallic quantum critical points have therefore attracted significant attention in recent years [1–11]. A different route towards the exploration of unconventional phase transitions has been the physics frustrated quantum magnets [12]. In the presence of significant quantum fluctuations arising from frustration, the system can feature fractionalized excitations, interacting via emergent gauge fields. Such a scenario has been heavily discussed at quantum phase transitions between Néel antiferromagnetic and valence bond solid phases in magnetic Mott insulators [13–23]. Since the two states adjacent to the phase transition point break different symmetries, a continuous and direct transition is, without fine tuning, not possible if the transition is governed by fluctuations of the order parameters alone. The numerical evidence for a generic continuous (or weakly first-order) transition has therefore been interpreted as a consequence of the emergence of fractionalized quasiparticle excitations that are confined in both long-range-ordered phases, but become deconfined at the transition point [24]. A related class of unconventional quantum critical points has been discussed in models that feature transitions into phases characterized by topological order, such as quantum spin liquids. If the fractionalized excitations associated with the topological order become or remain gapless at the transition point, they give rise to exotic fractionalized quantum universality classes that do not have any classical analogues [25–31].

In this paper, we study a lattice model that features two metallic quantum phase transitions as function of coupling strength [32]. The first one is continuous and can be understood within the $(2 + 1)$-dimensional Gross-Neveu-SO(3) [GN-SO(3)] field theory [33]. In the SO(3)-broken phase, two out of three Dirac cones acquire a mass, and the wave function of the ungapped Dirac electron couples to the SO(3) order parameter. Similar mass terms have been put forward in spin-orbit-coupled fermions on a honeycomb

lattice [34]. The second one is a transition between two long-range-ordered phases that break different symmetries: the aforementioned SO(3)-spin-symmetry-broken semimetal and a U(1)-charge-symmetry-broken fully gapped state [35]. The latter can be understood as an insulator characterized by U(1) interlayer coherence [32]. We show, nevertheless, that the interlayer-coherent insulator is degenerate with an s-wave superconducting state as a consequence of a partial particle-hole (PPH) symmetry. At the level of mean-field theory, the transition between the SO(3)-spin- and U(1)-charge-symmetry-broken phases is strongly first order [32]. Quantum fluctuations beyond mean-field theory significantly weaken this order-to-order transition, rendering it a candidate for a deconfined quantum critical point in the presence of gapless fermionic excitations—a potential microscopic realization of metallic deconfined quantum criticality [36]. We use large-scale sign-problem free quantum Monte Carlo (QMC) simulations with a Hermitian Trotter decomposition, which significantly improves convergence properties with respect to the limit of small Trotter time steps, to compute the quantum critical and thermodynamic properties of both transitions. Furthermore, in contrast to our initial exploratory study of this model [32], we employ a microscopic implementation that preserves the model's PPH symmetry explicitly, maintaining the degeneracy of the interlayer-coherent insulating and s-wave superconducting ground states in the fully gapped phase already on finite lattices. The interlayer-coherent insulating and s-wave superconducting states allow finite-temperature phases above the zero-temperature order. The latter breaks both U(1)-charge and PPH symmetries. Upon increasing temperature, it is therefore possible that the U(1) and PPH orders melt at different temperatures, with an intermediate vestigial phase at intermediate temperatures [37–39]. We compute the finite-temperature phase diagram of the model and show that the boundaries of the low-temperature orders vanish upon approaching the putative deconfined quantum critical point, in agreement with the expectation for a continuous or weak-first-order transition.

The rest of this paper is organized as follows: In Sec. II, we introduce our model. Its symmetries are discussed in Sec. III. Details of our QMC simulations, with a focus on the technical advances achieved in the present paper in comparison with our initial exploratory study of the model [32], are given in Sec. IV. Section V contains a discussion of our results on the critical properties of the two different quantum phase transitions occurring in our model at zero temperature. In Sec. VI, we present our results on the finite-temperature phase diagram of the model. We conclude with a summary and outlook in Sec. VII.

II. MODEL

We consider a model of interacting complex fermions on the bilayer honeycomb lattice, defined by the Hamiltonian

$$\hat{H} = \hat{H}_0 + \hat{H}_J \qquad (1)$$

with nearest-neighbor intralayer hopping part

$$\hat{H}_0 = -t \sum_{\langle ij \rangle} \hat{c}^\dagger_{i,\sigma,\lambda} \hat{c}_{j,\sigma,\lambda} \qquad (2)$$

with hopping parameter $t > 0$ and an SO(3)-symmetric on-site interaction part

$$\hat{H}_J = -J \sum_{i,\alpha} \left(\hat{c}^\dagger_{i,\sigma,\lambda} K^\alpha_{\sigma\sigma'} \tau^z_{\lambda\lambda'} \hat{c}_{i,\sigma',\lambda'} \right)^2. \qquad (3)$$

with coupling $J \geqslant 0$. Here, $\langle ij \rangle$ denotes nearest neighbors on the single honeycomb layer with $N = 2L \times L$ sites, $\lambda = 1, 2$ is the layer index, $\alpha = 1, 2, 3$ counts the three 3×3 generators $(K^\alpha)_{\sigma\sigma'} = -i\epsilon_{\alpha\sigma\sigma'}$ of SO(3), and $\sigma, \sigma' = 1, 2, 3$ count internal SO(3) degrees of freedom; the diagonal Pauli matrix τ^z acts on the layer degrees of freedom. The summation over repeated layer and SO(3) indices is implicitly assumed throughout the paper, unless specified otherwise.

The interacting fermion hopping model defined by $\hat{H}$ can be understood as an effective low-energy description of a frustrated Kugel-Khomskii-type spin-orbital model [30]. In the spin-orbital formulation, the fermionic quasiparticles created by $\hat{c}^\dagger_{i,\sigma,\lambda}$ represent spinons arising from fractionalization in a quantum spin-orbital liquid phase [40]. Moreover, in this formulation, the SO(3) vector $\hat{\vec{s}}_{i,\lambda} = (\hat{s}^\alpha_{i,\lambda})$ with components $\hat{s}^\alpha_{i,\lambda} := \sum_{\sigma,\sigma'} \hat{c}^\dagger_{i,\sigma,\lambda} K^\alpha_{\sigma\sigma'} \hat{c}_{i,\sigma',\lambda}$ (no summation over λ) describes the spin density on site i and layer λ. The interaction term $\hat{H}_J = -J \sum_i (\hat{\vec{s}}_{i,1} - \hat{\vec{s}}_{i,2})^2$ then favors differences in spin densities between the two layers, and can therefore be understood as a type of interlayer spin-density interaction. For simplicity, in what follows, we consistently refer to $\hat{H}_J$ as spin-density interaction, also in those cases in which no explicit reference to the model's spin-orbital formulation is made. A sketch of the model is depicted in Fig. 1(a).

The interacting bilayer honeycomb model defined by Eqs. (1)–(3) has previously been studied at zero temperature using mean-field theory and projective QMC simulations in Ref. [32]. The corresponding quantum phase diagram as function of interaction strength J, as obtained from Ref. [32], is schematically shown in the bottom panel of Fig. 1(b). The model features three different phases at zero temperature. At weak interaction $J < J_{c1}$, a fully symmetric Dirac semimetal (DSM) is realized. It features $3 \times 2 \times 2 = 12$ gapless Dirac cones at the Fermi level, arising from the spin, layer, and valley degrees of freedom. At intermediate interaction $J_{c1} < J < J_{c2}$, an SO(3)-spin-symmetry-broken Dirac semimetal (SO3 DSM) is stabilized, in which eight out of the 12 Dirac cones acquire a mass gap, while the four leftover Dirac cones remain gapless. This partial gap opening is a consequence of the zero eigenvalue of the SO(3) generators $K^\alpha_{\sigma\sigma'}$. At strong interaction $J > J_{c2}$, a U(1)-charge-symmetry-broken fully gapped state is stabilized. It can be understood as an insulator characterized by U(1) interlayer coherence [32]; however, we show below that the interlayer-coherent insulator (ILC) is degenerate with an s-wave superconducting state (SSC) as a consequence of a PPH symmetry. The fermion single-particle spectral function from mean-field theory [32] is shown for representative values within the three different phases in the top panel of Fig. 1(b), illustrating the partial and full gap opening at intermediate and strong coupling, respectively.

III. SYMMETRIES

The model's rich phase diagram originates from the large number of fermion internal degrees of freedom together with
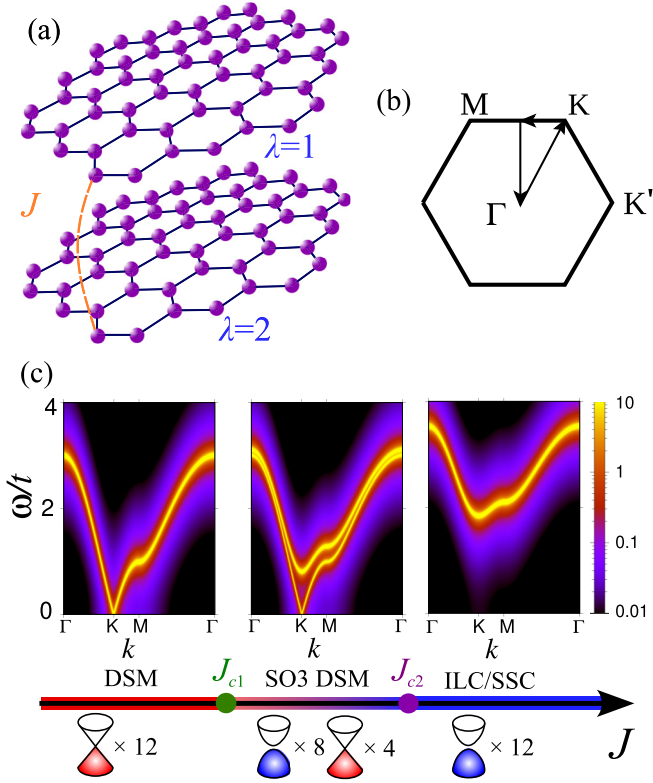
FIG. 1. (a) Sketch of bilayer honeycomb model defined by the Hamiltonian given in Eqs. (1)–(3). Each lattice site (purple dots) contain three SO(3) spin flavor degrees of freedom. The two layers interact via an SO(3)-symmetric spin-density interaction parametrized by the coupling J (orange link). (c) (Bottom) Schematic quantum phase diagram as function of J, showing the disordered Dirac semimetal (DSM) at small J, the SO(3)-spin-symmetry-broken Dirac semimetal (SO3 DSM), in which 2/3 of the Dirac cones acquire a mass gap, while 1/3 remains gapless, at intermediate J, as well as the fully gapped degenerate interlayer-coherent insulator (ILC) and s-wave superconductor (SSC) at strong J. The insets illustrate the fermion band structures in the three different phases. (Top) Fermion single-particle spectral function from lattice mean-field theory along a high-symmetry path in the first Brillouin zone [depicted in (b)], illustrating the partial and full gap openings in the SO3 DSM and ILC/SSC phases, respectively.

the intricate symmetry structure. In the following, we analyze in detail the symmetries of the hopping and interaction parts of the Hamiltonian defined in Eqs. (2) and (3), respectively. It will prove convenient to do this using a Majorana fermion representation.

A. Majorana representation

We introduce two Majorana fermions $\hat{\gamma}_{i,\sigma,\lambda,1}$ and $\hat{\gamma}_{i,\sigma,\lambda,2}$ for each complex fermion $\hat{c}_{i,\sigma,\lambda}$ on the two different sublattices A and B as

$$\hat{c}_{i,\sigma,\lambda} = \begin{cases} \frac{1}{2}(\hat{\gamma}_{i,\sigma,\lambda,1} - \mathrm{i}\hat{\gamma}_{i,\sigma,\lambda,2}), & \text{if } i \in A, \\ \frac{1}{2}(\hat{\gamma}_{i,\sigma,\lambda,1} - \mathrm{i}\hat{\gamma}_{i,\sigma,\lambda,2}), & \text{if } i \in B. \end{cases} \quad (4)$$

The Hermitian Majorana operators obey the anticommutation relation $\{\hat{\gamma}_{i,\sigma,\lambda,l}, \hat{\gamma}_{j,\sigma',\lambda',l'}\} = 2\delta_{ij}\delta_{\sigma\sigma'}\delta_{\lambda\lambda'}\delta_{ll'}$, where $l = 1, 2$ corresponds to the Majorana index. Introducing a

twelve-component spinor $\hat{\vec{\gamma}}_i^\top = (\hat{\gamma}_{i,\sigma,\lambda,l})$, obtained by combining the spin, layer, and Majorana indices into one super-index, allows us to write the kinetic energy $\hat{H}_0$ as

$$\hat{H}_0 = \frac{\mathrm{i}t}{4} \sum_{\langle ij \rangle} \hat{\vec{\gamma}}_i^\top \hat{\vec{\gamma}}_j. \quad (5)$$

In this form, the hopping part of the Hamiltonian becomes manifestly invariant under O(12) rotations, under which the Majorana spinor transforms as a vector,

$$\hat{\vec{\gamma}}_i \mapsto \hat{\vec{\gamma}}_i' = O\hat{\vec{\gamma}}_i, \quad \text{with } O^\top O = \mathbb{1}_{12}. \quad (6)$$

The on-site interaction term becomes in the Majorana formulation

$$\begin{aligned} &\left(\hat{c}_{i,\sigma,\lambda}^\dagger K_{\sigma,\sigma'}^\alpha \tau_{\lambda,\lambda'}^z \hat{c}_{i,\sigma',\lambda'}\right)^2 \\ &= \frac{1}{4}\left[(\hat{\gamma}_{i,\sigma,\lambda,1} + \mathrm{i}\hat{\gamma}_{i,\sigma,\lambda,2})K_{\sigma\sigma'}^\alpha \tau_{\lambda\lambda'}^z (\hat{\gamma}_{i,\sigma',\lambda',1} - \mathrm{i}\hat{\gamma}_{i,\sigma',\lambda',2})\right]^2 \\ &= \frac{1}{4}\left(\hat{\gamma}_{i,\sigma,\lambda,l}K_{\sigma\sigma'}^\alpha \tau_{\lambda\lambda'}^z \hat{\gamma}_{i,\sigma',\lambda',l}\right)^2 \\ &= \frac{1}{4}\left(\hat{\vec{\gamma}}_i^\top K^\alpha \tau^z \mu^0 \hat{\vec{\gamma}}_i\right)^2, \end{aligned} \quad (7)$$

where, in the last step, we have introduced the identity matrix $\mu^0 := \mathbb{1}_2$ that acts on the Majorana flavor index. We recall that τ^z acts on the layer index and the SO(3) generators K^α, $\alpha = 1, 2, 3$, act on the spin indices. In the above, the cross terms in the Majorana index vanish since the K^α are antisymmetric and τ^z is symmetric.

All in all, the full Hamiltonian takes the form

$$\hat{H} = \frac{\mathrm{i}t}{4} \sum_{\langle ij \rangle} \hat{\vec{\gamma}}_i^\top \hat{\vec{\gamma}}_j - \frac{J}{4} \sum_{i,\alpha} \left(\hat{\vec{\gamma}}_i^\top K^\alpha \tau^z \mu^0 \hat{\vec{\gamma}}_i\right)^2. \quad (8)$$

The interaction term reduces the O(12) global symmetry of the hopping term down to a subgroup that satisfies

$$O^\top K^\alpha \tau^z \mu^0 O = R^{\alpha\beta} K^\beta \tau^z \mu^0, \quad (9)$$

where R is an SO(3) matrix and the sum over repeated spin indices is implicitly implied. We can now systematically read off the global symmetries of our Hamiltonian.

B. SO(3) spin rotational symmetry

Here,

$$O_{\mathrm{SO(3)}} = \mathrm{e}^{\mathrm{i}\theta\vec{e}\cdot\vec{K}}, \quad (10)$$

with rotation angle $\theta \in [0, 2\pi)$ and rotation axis $\vec{e}$, and a similar form holds for R. Since $O_{\mathrm{SO(3)}}^\top = O_{\mathrm{SO(3)}}^\dagger$, the complex fermion operators transform as

$$\hat{c}_{i,\sigma,\lambda} \mapsto (O_{\mathrm{SO(3)}})_{\sigma\sigma'}\hat{c}_{i,\sigma',\lambda}. \quad (11)$$

The SO(3) order parameter reads

$$\hat{\vec{S}}_i = (\hat{S}_i^\alpha) := \hat{c}_{i,\sigma,\lambda}^\dagger K_{\sigma\sigma'}^\alpha \hat{c}_{i,\sigma',\lambda}, \quad (12)$$

which can be understood as total spin density, $\hat{\vec{S}}_i = \hat{\vec{s}}_{i,1} + \hat{\vec{s}}_{i,2}$, where $\hat{\vec{s}}_{i,\lambda}$ denotes the spin density at site i on layer λ. The spin density $\hat{\vec{S}}_i$ transforms as a vector under SO(3) rotations.

C. U(1) total-charge symmetry

Here,

$$O_{\mathrm{U(1)_T}} = \mathrm{e}^{\mathrm{i}\theta\mu^y} \tag{13}$$

and $R = 1$. In the above, μ^y corresponds to the second Pauli matrix that acts on the Majorana flavor index. For $i \in A$, we have

$$\hat{c}_{i,\sigma,\lambda} = \tfrac{1}{2}(\hat{\gamma}_{i,\sigma,\lambda,1} - \mathrm{i}\hat{\gamma}_{i,\sigma,\lambda,2}) \mapsto \mathrm{e}^{\mathrm{i}\theta}\hat{c}_{i,\sigma,\lambda}, \tag{14}$$

and a similar form holds for $i \in B$. A possible order parameter for U(1) total-charge symmetry breaking is the interlayer s-wave pairing operator $\hat{\Delta}_i := \hat{c}^\dagger_{i,\sigma,1}\hat{c}^\dagger_{i,\sigma,2}$.

D. U(1) layer-charge symmetry

Here,

$$O_{\mathrm{U(1)_L}} = \mathrm{e}^{\mathrm{i}\theta\tau^z\mu^y} \tag{15}$$

and $R = 1$. This symmetry reflects the fact that the charge is conserved separately on each layer. For the fermion operator, the symmetry transformation reads

$$\hat{c}_{i,\sigma,\lambda} \mapsto (\mathrm{e}^{\mathrm{i}\theta\tau^z})_{\lambda\lambda'}\hat{c}_{i,\sigma,\lambda'}. \tag{16}$$

An order parameter for spontaneous U(1) layer-charge symmetry breaking is given by the interlayer coherence operator $\hat{n}^\dagger_i := \hat{c}^\dagger_{i,\sigma,1}\hat{c}_{i,\sigma,2}$.

E. $\mathbb{Z}_2$ partial particle-hole (PPH) symmetry

Here,

$$O_{\mathrm{PPH}} = \frac{1 + \tau^z}{2} + \frac{1 - \tau^z}{2}\mu^z \tag{17}$$

and $R = 1$. The PPH symmetry is a $\mathbb{Z}_2$ symmetry since $O^2_{\mathrm{PPH}} = 1$. It acts solely on the second layer where $\tau^z_{2,2} = -1$. In the fermion representation, it leads to

$$\hat{c}_{i,\sigma,1} \mapsto \hat{c}_{i,\sigma,1}, \quad \text{for all } i \in A, B, \tag{18}$$

$$\hat{c}_{i,\sigma,2} \mapsto \begin{cases} \hat{c}^\dagger_{i,\sigma,2}, & \text{if } i \in A, \\ -\hat{c}^\dagger_{i,\sigma,2}, & \text{if } i \in B, \end{cases} \tag{19}$$

While $\det(O_{\mathrm{SO(3)}}) = \det(O_{\mathrm{U(1)_T}}) = \det(O_{\mathrm{U(1)_L}}) = 1$, one will show that $\det(O_{\mathrm{PPH}}) = -1$. A possible order parameter that probes PPH symmetry breaking hence reads

$$\hat{P}_i := \prod_{\sigma,\lambda,l} \gamma_{i,\sigma,\lambda,l}, \tag{20}$$

since under O(12) transformations $\hat{P}_i \mapsto \det(O)\hat{P}_i$. In fermion notation, we find

$$\hat{P}_i = \prod_{\sigma,\lambda}(1 - 2\hat{c}^\dagger_{i,\sigma,\lambda}\hat{c}_{i,\sigma,\lambda}). \tag{21}$$

(In the above equation, there is no summation over σ, λ.) Under the PPH transformation, the interlayer-coherent insulator thus maps onto an s-wave superconductor and vice versa. These two states are therefore degenerate by symmetry. Long-range order in the U(1) layer-charge symmetry broken sector thus implies long-range order in the U(1) total-charge sector. We note that the insertion of a flux quantum, as done in our previous paper [32], breaks the PPH symmetry, and as such

lifts on finite lattices the degeneracy between the interlayer-coherent insulator and the s-wave superconductor in favor of the insulating state. In this paper, we therefore refrain from inserting a flux quantum, such that the PPH-symmetry-required degeneracy remains intact already on finite lattices.

IV. QMC SIMULATIONS

In this section, we present aspects of our QMC simulations. It is beyond the scope of this article to provide a detailed account of the algorithm and we will concentrate on model specific issues. We start by describing two different possible Trotter decompositions, demonstrate the absence of the sign problem, describe the specific implementation, and finally illustrate the convergence properties with respect to the limit of small Trotter time steps of the two different decompositions.

A. Trotter decomposition

We represent the partition function at inverse temperature β as

$$Z = \mathrm{Tr} \prod_{n=1}^{M} \exp(-\Delta\tau\hat{H}), \tag{22}$$

where M corresponds to the number of Trotter time steps $\Delta\tau = \beta/M$.

(a) Naive Trotter decomposition. For sufficiently large $M \gg 1$, the partition function can be decomposed as

$$\exp(-\Delta\tau\hat{H}) = \int \mathcal{D}\vec{\phi}\, \mathrm{e}^{-\sum_i \frac{\vec{\phi}^2_{i,\tau}}{2}} \mathrm{Tr} \prod_{n=1}^{M}\left\{ \mathrm{e}^{-\frac{\Delta\tau}{2}\hat{H}_0} \right.$$
$$\left. \times \left(\prod_{\alpha=1}^{3} \mathrm{e}^{-\sum_{i,j}\hat{c}^\dagger_{i,\lambda}V^\alpha_{ij}(\vec{\phi})\tau^z_{\lambda\lambda'}\hat{c}_{j,\lambda'}}\right) \mathrm{e}^{-\frac{\Delta\tau}{2}\hat{H}_0} \right\}$$
$$+ \mathcal{O}(\Delta\tau^2), \tag{23}$$

where the functional integral $\int \mathcal{D}\vec{\phi}$ is assumed over the auxiliary fields $\vec{\phi}_{i,\tau} = (\phi^\alpha_{i,\tau})$, and we have introduced $V^\alpha_{ij}(\vec{\phi}) = \sqrt{2\Delta\tau J}\delta_{ij}\phi^\alpha_{i,\tau}K^\alpha$ and $\hat{\mathbf{c}}_{i,\lambda} = (\hat{c}_{i,\sigma,\lambda})$. The partition function can then be represented in terms of a fermion determinant as

$$Z = \int \mathcal{D}\vec{\phi}\,\mathrm{e}^{-\sum_i \frac{\vec{\phi}^2_{i,\tau}}{2}} \det W(\vec{\phi}) \tag{24}$$

with the fermion matrix given as

$$W(\vec{\phi}) = \mathbb{1} + \prod_{n=1}^{M}\left\{ \mathrm{e}^{-\frac{\Delta\tau}{2}T}\left(\prod_{\alpha=1}^{3}\mathrm{e}^{-V^\alpha(\vec{\phi})}\right)\mathrm{e}^{-\frac{\Delta\tau}{2}T} \right\}. \tag{25}$$

Here, $V^\alpha = (V^\alpha_{ij})\tau^z$ corresponds to the vertex matrix and $T = (T_{ij})\tau^0$ corresponds to the hopping matrix, with elements $T_{ij} = -t$ if i and j are nearest neighbors and $T_{ij} = 0$ otherwise, and the identity matrix $\tau^0 = \mathbb{1}_2$ acts on the layer degrees of freedom. As the generators of SO(3), K^α, $\alpha = 1, 2, 3$, do not commute with each other, the naive Trotter decomposition in Eq. (23) leads to a Hermitian time evolution only in the limit $M \to \infty$.

(b) Hermitian Trotter decomposition. A Hermitian time evolution already at finite M can be achieved at the expense

of introducing another set of auxiliary fields $\vec{\chi}$ in a symmetric Trotter decomposition as

$$\exp(-\Delta\tau\hat{H}) = \int \mathcal{D}\vec{\phi}\mathcal{D}\vec{\chi}\, e^{-\sum_i \frac{\vec{\phi}_{i,\tau}^2 + \vec{\chi}_{i,\tau}^2}{2}} \operatorname{Tr} \prod_{n=1}^{M} \left\{ e^{-\frac{\Delta\tau}{2}\hat{H}_0} \right.$$

$$\times \left(\prod_{\alpha=1}^{3} e^{-\sum_{i,j} \frac{1}{2}\hat{\mathfrak{c}}_i^\dagger V_{ij}^\alpha(\vec{\phi})\hat{\mathfrak{c}}_j} \right)$$

$$\times \left. \left(\prod_{\beta=3}^{1} e^{-\sum_{i,j} \frac{1}{2}\hat{\mathfrak{c}}_i^\dagger V_{ij}^\beta(\vec{\chi})\hat{\mathfrak{c}}_j} \right) e^{-\frac{\Delta\tau}{2}\hat{H}_0} \right\}$$

$$+ \mathcal{O}(\Delta\tau^2). \tag{26}$$

The partition function can then analogously be represented in terms of a fermion determinant $\det W(\vec{\phi}, \vec{\chi})$, with the corresponding fermion matrix given as

$$W(\vec{\phi}, \vec{\chi}) = \mathbb{1} + \prod_{n=1}^{M} \left\{ e^{-\frac{\Delta\tau T}{2}} \left(\prod_{\alpha=1}^{3} e^{-\frac{V^\alpha(\vec{\phi})}{2}} \right) \left(\prod_{\beta=3}^{1} e^{-\frac{V^\beta(\vec{\chi})}{2}} \right) \right.$$

$$\left. \times e^{\frac{-\Delta\tau T}{2}} \right\}. \tag{27}$$

Below, we show that the above Hermitian Trotter decomposition leads to significantly improved convergence properties towards the $M \to \infty$ limit.

B. Absence of sign problem

For simplicity, we show the absence of the sign problem for the naive Trotter decomposition with the fermion determinant $\det W(\vec{\phi})$. Analogous arguments hold for the Hermitian Trotter decomposition with the fermion determinant $\det W(\vec{\phi}, \vec{\chi})$.

In our model, the hopping matrix T and the vertex matrix $V^\alpha(\vec{\phi})$ are block diagonal with respect to the layer index, such that the fermion determinant can be written as a product of single-layer fermion determinants as

$$\det W(\vec{\phi}) = \det W_1(\vec{\phi}) \det W_2(\vec{\phi}), \tag{28}$$

where W_λ corresponds to the fermion matrix on the λth layer, $\lambda = 1, 2$,

$$W_\lambda(\vec{\phi}) = \mathbb{1} + \prod_{n=1}^{M} \left\{ e^{\frac{-\Delta\tau(T_{ij})}{2}} \left(\prod_{\alpha=1}^{3} e^{(-1)^\lambda(V_{ij}^\alpha)(\vec{\phi})} \right) e^{\frac{-\Delta\tau(T_{ij})}{2}} \right\}, \tag{29}$$

where the $N \times N$ matrices (T_{ij}) and (V_{ij}^α) act only on a single layer. As the hopping matrix is real, $(T_{ij})^* = (T_{ij})$, and the vertex matrix purely imaginary, $(V_{ij}^\alpha)^* = -(V_{ij}^\alpha)$, we have $[\det W_1(\vec{\phi})]^* = \det W_2(\vec{\phi})$ for all real configurations $\vec{\phi}$. As a consequence, the fermion determinant is nonnegative,

$$\det W(\vec{\phi}) \geqslant 0, \tag{30}$$
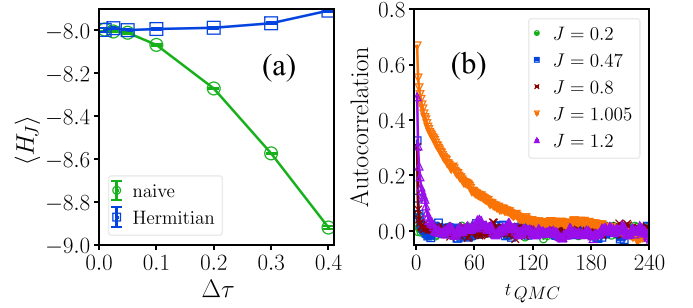
facilitating sign-problem-free QMC simulations.

FIG. 2. (a) Expectation value of the interaction part of the Hamiltonian $\langle\hat{H}_J\rangle$ as function of Trotter time step $\Delta\tau$ for the two different Trotter decompositions, using $t = 0$, $J = 1$, and $\beta = 4$. The Hermitian Trotter decomposition leads to significantly improved convergence properties towards the limit $\Delta\tau = \beta/M \to 0$. (b) Autocorrelation function of hopping part of the Hamiltonian $\langle\hat{H}_0\rangle$ as function of Monte Carlo time t_{QMC} for different fixed values of J, using $L = 6$ and $\beta = 18$. The autocorrelation time remains small near the GN-SO(3) transition point at $J_{c1} = 0.465(2)$, but significantly increases in the vicinity of the SO(3)-U(1) transition point at $J_{c2} = 1.057(10)$.

C. Specific implementation

We use the ALF implementation [41] of the auxiliary field QMC algorithm [42–45]. This package utilizes Gauss-Hermite quadrature to replace sampling over continuous fields with a discrete field that takes the values ± 2 and ± 1. For further details, we refer to Refs. [41,46]. While both approaches are formally equivalent, sampling over discrete fields generally reduces fluctuations. Our finite inverse temperature β calculations are carried out in the grand-canonical ensemble, choosing linear system sizes $L = 6, 9, 12, 15, 18$ with periodic boundary conditions. For the zero-temperature results, we adopt a $\beta = L$ scaling, consistent with a dynamical critical exponent $z = 1$, as naively expected from the linear fermion dispersion. If not stated otherwise, we use a Trotter time step of $\Delta\tau = 0.2$. We choose units in which $t = 1$ and $k_B = 1$, such that the temperature $T = 1/\beta$ and the coupling constant $J \geqslant 0$ become dimensionless parameters, which we scan.

D. Convergence of Trotter decomposition

Figure 2(a) shows the expectation value of the interaction part of the Hamiltonian $\langle\hat{H}_J\rangle$ as function of the Trotter time step $\Delta\tau$ for the two different Trotter decompositions. Importantly, the Hermitian decomposition leads, in comparison with the naive decomposition, to significantly improved convergence properties towards the limit $\Delta\tau = \beta/M \to 0$. In the remainder of this paper, we therefore exclusively employ the Hermitian Trotter decomposition. As shown below, this allows us to obtain significantly improved estimates for the quantum critical properties at zero temperature in comparison with our previous paper [32].

V. ZERO-TEMPERATURE RESULTS

In this section, we demonstrate that the above-described advances in the implementation of our model leads, in comparison with our previous paper [32], to significant
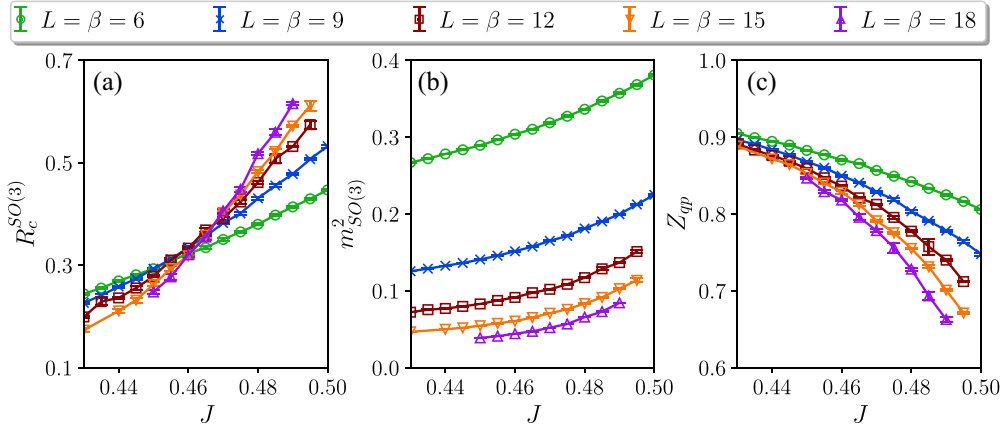
FIG. 3. (a) SO(3) correlation ratio $R_c^{SO(3)}$ as function of coupling J in the vicinity of the GN-SO(3) transition for different fixed lattice sizes L. The crossing point of the different finite-size curves indicates the location of the GN-SO(3) quantum critical point. (b) Same as (a), but for the SO(3) order parameter $m_{SO(3)}^2$. (c) Same as (a), but for the fermion quasiparticle weight Z_{qp}.

improvements in the results obtained at zero temperature. This is in particular true in the vicinity of the two quantum phase transition points.

A. GN-SO(3) transition

We start by discussing the GN-SO(3) transition at J_{c1} between the fully symmetric Dirac semimetal and SO(3)-spin-symmetry-broken partially gapped Dirac semimetal. To this end, we measure the SO(3) order parameter $m_{SO(3)}$ defined via

$$m_{SO(3)}^2(J, L) = \frac{\mathcal{S}_{SO(3)}(\boldsymbol{k} = \boldsymbol{\Gamma}, \tau = 0)}{L^2}, \quad (31)$$

where

$$\mathcal{S}_{SO(3)}(\boldsymbol{k}, \tau) = \sum_i e^{-i\boldsymbol{k} \cdot \boldsymbol{r}_i} \langle \hat{\vec{s}}_{i,\lambda}(\tau) \cdot \hat{\vec{s}}_{0,\lambda}(0) \rangle \quad (32)$$

is the SO(3) spin structure factor at momentum $\boldsymbol{k}$ and imaginary time τ, and $\boldsymbol{r}_i$ denotes the position vector of the lattice site i. The spin structure factor describes correlations between the spin density $\hat{\vec{s}}_{i,\lambda}(\tau) = \hat{\mathbf{c}}_{i,\lambda}^\dagger(\tau) \vec{K} \hat{\mathbf{c}}_{i,\lambda}(\tau)$ (no summation over λ), where $\hat{\mathbf{c}}_{i,\lambda}^\dagger(\tau)$ is the time-evolved fermion operator in the Heisenberg picture. In order to locate the GN-SO(3) transition, we compute the renormalization group invariant SO(3) correlation ratio [47]

$$R_c^{SO(3)}(J, L) = 1 - \frac{\mathcal{S}_{SO(3)}(\boldsymbol{k} = \boldsymbol{\Gamma} + d\boldsymbol{k}, \tau = 0)}{\mathcal{S}_{SO(3)}(\boldsymbol{k} = \boldsymbol{\Gamma}, \tau = 0)}, \quad (33)$$

where $d\boldsymbol{k}$ connects neighboring momenta in the Brillouin zone of the finite-size lattice. In the limit of large system size, the correlation ratio $R_c^{SO(3)}$ goes to zero (one) in the SO(3)-ordered (disordered) phase. The crossings of the correlation-ratio curves as function of the tuning parameter J for different fixed lattices sizes L indicate the location of the SO(3)-spin-symmetry-breaking phase transition. In addition, we measure the fermion quasiparticle weight

$$Z_{qp}(J, L) = \frac{G(J, L)}{G(0, L)} \quad (34)$$

where $G(J, L)$ is constructed from the time dependence of the fermion Green's function as

$$G(J, L) = \langle \hat{\mathbf{c}}_{i,\lambda}^\dagger(\beta/2) \cdot \hat{\mathbf{c}}_{i,\lambda}(0) \rangle. \quad (35)$$

Figure 3 shows the raw data of these three observables near the GN-SO(3) quantum phase transition. For the correlation ratio [Fig. 3(a)], we observe a clear crossing point, indicating the position of the GN-SO(3) quantum critical point. Following the finite-size scaling hypothesis [48], the observables are expected to obey the critical scaling form

$$R_c^{SO(3)}(J, L) \sim f_0^R(jL^{1/\nu}) + L^{-\omega} f_1^R(jL^{1/\nu}), \quad (36)$$

$$m_{SO(3)}^2(J, L) \sim L^{-1-\eta_\phi} [f_0^m(jL^{1/\nu}) + L^{-\omega} f_1^m(jL^{1/\nu})], \quad (37)$$

$$Z_{qp}(J, L) \sim L^{-\eta_\psi} [f_0^z(jL^{1/\nu}) + L^{-\omega} f_1^z(jL^{1/\nu})], \quad (38)$$

where $j = J - J_{c1}$ corresponds to the reduced coupling and ω denotes the correction-to-scaling exponent. We use two different types of finite-size analysis in order to extract the critical coupling and the corresponding exponents. The two methods lead to results that are consistent within the numerical uncertainty.

(a) Data-collapse analysis. As a first step, we ignore the corrections to scaling $\propto \mathcal{O}(L^{-\omega})$ in the above finite-size scaling forms. In order to extract the critical coupling J_{c1} and the correlation-length exponent ν, we fit the correlation ratio $R_c^{SO(3)}(J, L)$ as function of $(J - J_{c1})L^{1/\nu}$ to a fourth-order polynomial. The optimal scaling collapse is obtained for the best-fit parameters $J_{c1} = 0.465(2)$ and $1/\nu = 0.86(8)$, see Fig. 4(a). From the finite-size scalings of the order parameter $m_{SO(3)}^2(j, L)$ and the $Z_{qp}(j, L)$, we analogously obtain the estimates $\eta_\phi = 0.73(2)$ for the order-parameter anomalous dimension and $\eta_\psi = 0.078(8)$ for the fermion anomalous dimension, respectively. The corresponding scaling collapses are shown in Figs. 4(b) and 4(c).

(b) Crossing-point analysis. As a second step, we compare the above results of the scaling-collapse analysis with those of a crossing-point analysis that takes scaling-correction effects into account [17]. We define the finite-size critical coupling $J_{c1}(L)$ as the crossing point of the SO(3) correlation ratio $R_c^{SO(3)}(J, L)$ of system sizes L and $L + c$ with size
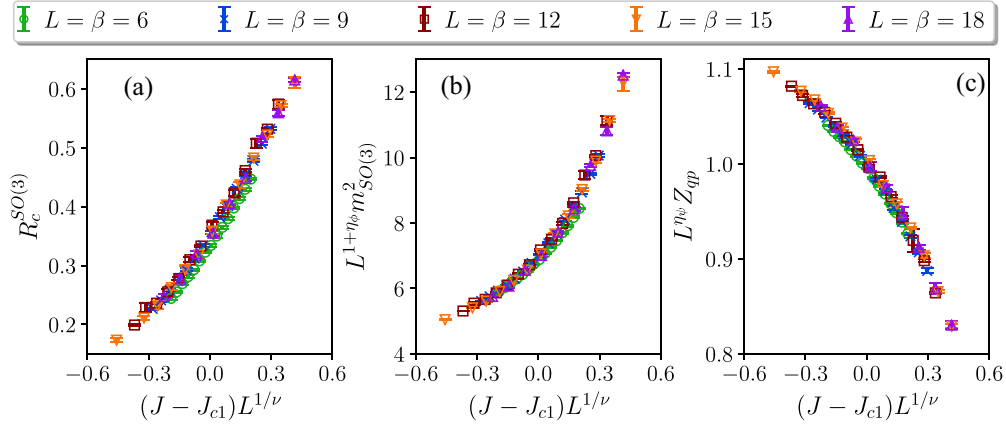
FIG. 4. (a) Finite-size scaling collapse of SO(3) correlation ratio as function of $(J - J_{c1})L^{1/\nu}$ in the vicinity of the GN-SO(3) transition, yielding the best-fit parameters $J_{c1} = 0.465(2)$ and $1/\nu = 0.86(8)$. (b) Same as (a), but for the order parameter $m_{SO(3)}^2$ in units of $L^{-1-\eta_\phi}$, yielding $\eta_\phi = 0.73(2)$. (c) Same as (a), but for the fermion quasiparticle weight Z_{qp} in units of $L^{-\eta_\psi}$, yielding $\eta_\psi = 0.078(8)$.

increment c as

$$R_c^{SO(3)}(J_{c1}(L), L) = R_c^{SO(3)}(J_{c1}(L), L + c). \tag{39}$$

For increasing system sizes, the finite-size critical coupling approaches the thermodynamic critical point as $J_{c1}(L) = J_{c1} + aL^{-\omega - 1/\nu}$, with nonuniversal coefficient a [49]. Figure 5(a) shows the finite-size critical coupling as function of $1/L$ for two different size increments (orange diamonds and blue squares) in comparison with the critical coupling
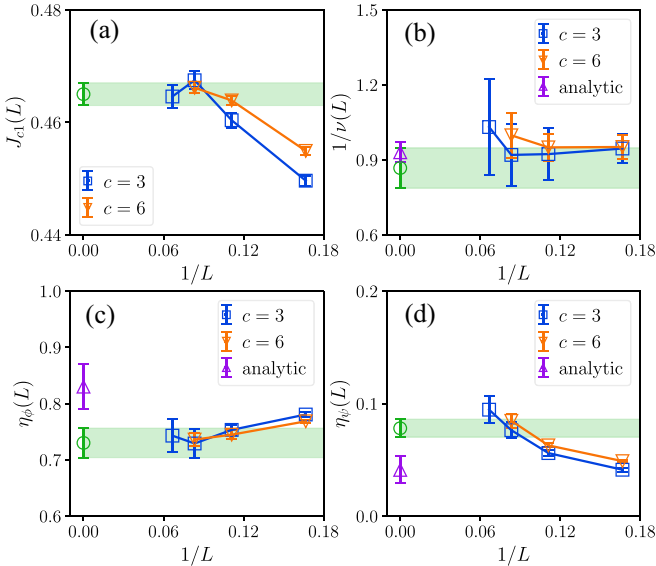

FIG. 5. (a) Finite-size critical coupling $J_{c1}(L)$ as function of $1/L$ from crossing-point analysis using size increments $c = 3$ (blue squares) and $c = 6$ (orange diamonds), respectively, in comparison with the critical coupling J_{c1} obtained from the data-collapse analysis (green dot). For sufficiently large lattice sizes, the estimates are consistent with each other within the numerical uncertainty. (b) Same as (a), but for the effective correlation-length exponent $1/\nu(L)$. (c) Same as (a), but for the effective order-parameter anomalous dimension $\eta_\phi(L)$. (d) Same as (a), but for the effective fermion anomalous dimension $\eta_\psi(L)$. Purple triangles in (b)–(d) show the field-theoretical estimates from Ref. [33] for comparison.

obtained from the data-collapse analysis (green circle). For sufficiently large lattice sizes, the estimates are consistent with each other within the numerical uncertainty.

Having computed the finite-size critical coupling, effective finite-size critical exponents can be obtained from

$$1/\nu(L) = \ln \frac{s(J_{c1}(L), L + c)}{s(J_{c1}(L), L)} \Big/ \ln \frac{L + c}{L}, \tag{40}$$

$$\eta_\phi(L) = -1 - \ln \frac{m_{SO(3)}^2(J_{c1}(L), L + c)}{m_{SO(3)}^2(J_c(L), L)} \Big/ \ln \frac{L + c}{L}, \tag{41}$$

$$\eta_\psi(L) = -\ln \frac{Z_{qp}(J_{c1}(L), L + c)}{Z_{qp}(J_{c1}(L), L)} \Big/ \ln \frac{L + c}{L}, \tag{42}$$

where $s(J, L) = \partial R_c^{SO(3)}(J, L)/\partial J$ corresponds to the slope of the correlation ratio as function of the coupling J. For increasing system sizes L, the deviation between the effective critical exponent and the corresponding value in the thermodynamic limit vanishes with $L^{-\omega}$. Our results for the effective finite-size critical exponents as function of $1/L$ for two different size increments (blue squares and orange diamonds) in comparison with the critical exponents obtained from the data-collapse analysis (green circles) are shown in Figs. 5(b)–5(d). For sufficiently large lattice sizes, the estimates from the different analyses are again consistent with each other within the numerical uncertainty.

From the symmetry of the order parameter and the low-energy field content of the lattice model, we expect the continuous quantum phase transition at J_{c1} to be described by the GN-SO(3) field theory [30] given by the action $S = \int d^3x \mathcal{L}$ with

$$\mathcal{L} = \bar{\Psi}\gamma^\mu \partial_\mu \Psi - g\vec{\phi} \cdot \bar{\Psi}(\mathbb{1}_4 \otimes \vec{K})\Psi, \tag{43}$$

where $\vec{\phi} = (\phi^\alpha)$, $\alpha = 1, 2, 3$, corresponds to the SO(3) vector order parameter and the complex fermion fields Ψ and $\bar{\Psi}$ have $2^3 \times 3 = 24$ components, arising from sublattice, valley, layer, and internal SO(3) degrees of freedom. The Dirac matrices γ^μ, $\mu = 0, 1, 2$, form a 24-dimensional representation of the Clifford algebra, and the summation convention over repeated space-time indices μ is assumed. The GN-SO(3) field theory has previously been studied using three-loop $4 - \epsilon$

expansion, next-to-leading-order $1/N$ expansion, and functional renormalization group calculations in the local-potential approximation [33]. The corresponding estimates for the critical exponents from combining these analytical methods are also shown in Figs. 5(b)–5(d) for comparison (purple triangles). Importantly, in comparison with our previous paper [32], in which the naive Trotter decomposition has been employed, the improved implementation using the Hermitian Trotter decomposition leads to results that are significantly closer to the field-theoretical estimates, in particular for the anomalous dimensions η_ϕ and η_ψ. We attribute the remaining small deviations of the order of $\lesssim 2\sigma$ to systematic uncertainties that are difficult to control within both field-theoretical and numerical approaches.

B. SO(3)-U(1) transition

We continue by describing the behavior of the system near the potentially deconfined metallic transition at J_{c2} between the SO(3)-spin- and U(1)-charge-symmetry-broken states. Across this transition, the remaining gapless fermion modes acquire a spectral gap. In order to characterize the transition, we compute both the SO(3) spin structure factor $\mathcal{S}_{SO(3)}(\boldsymbol{k}, \tau)$ and the U(1) layer-charge structure factor, defined as

$$\mathcal{S}_{U(1)}(\boldsymbol{k}, \tau) = \sum_i e^{-i\boldsymbol{k}\cdot\boldsymbol{r}_i} \langle [\hat{n}_i^\dagger(\tau) + \hat{n}_i(\tau)][\hat{n}_0^\dagger(0) + \hat{n}_0(0)] \rangle,$$
(44)

where $n_i^\dagger(\tau) = \hat{c}_{i,\sigma,1}^\dagger(\tau)\hat{c}_{i,\sigma,2}(\tau)$ corresponds to the interlayer coherence operator in the Heisenberg picture. Under the PPH transformation, the U(1) layer-charge structure factor transforms into the U(1) pairing structure factor

$$\mathcal{S}'_{U(1)}(\boldsymbol{k}, \tau) = \sum_i e^{-i\boldsymbol{k}\cdot\boldsymbol{r}_i} \langle [\hat{\Delta}_i^\dagger(\tau) + \hat{\Delta}_i(\tau)][\hat{\Delta}_0^\dagger(0) + \hat{\Delta}_0(0)] \rangle,$$
(45)

where $\Delta_i(\tau) = \hat{c}_{i,\sigma,1}^\dagger(\tau)\hat{c}_{i,\sigma,2}^\dagger(\tau)$ corresponds to the interlayer s-wave pairing operator in the Heisenberg picture. In this paper, we use a microscopic implementation that explicitly preserves PPH symmetry. As a consequence, our results presented for $\mathcal{S}_{U(1)}(\boldsymbol{k}, \tau)$ in the following are representative for both the U(1) layer-charge and U(1) pairing structure factors. The U(1) correlation ratio is defined as

$$R_c^{U(1)}(J, L) = 1 - \frac{\mathcal{S}_{U(1)}(\boldsymbol{k} = \boldsymbol{\Gamma} + d\boldsymbol{k}, \tau = 0)}{\mathcal{S}_{U(1)}(\boldsymbol{k} = \boldsymbol{\Gamma}, \tau = 0)},$$
(46)

Analogously, we define the PPH structure factor $\mathcal{S}_{PPH}(\boldsymbol{k}, \tau)$ and the corresponding correlation ratio R_c^{PPH} using the parity operator $\hat{P}_i(\tau) = \prod_{\sigma,\lambda}[1 - 2\hat{c}_{i,\sigma,\lambda}^\dagger(\tau)\hat{c}_{i,\sigma,\lambda}(\tau)]$ (no summation over σ, λ).

Figures 6(a)–6(c) show our results for the SO(3), U(1) and PPH correlation ratios. These observables indicate a phase transition between the partially gapped SO(3)-spin-symmetry-broken semimetal at $J_{c1} < J < J_{c2}$ and the interlayer-coherent insulating or s-wave superconducting state, which breaks U(1)-charge and PPH symmetries, at $J > J_{c2}$. This interpretation is also supported by the finite-size scaling of the correlation-ratio crossing points for consecutive system sizes, shown as function of $1/L$ in Fig. 6(d).
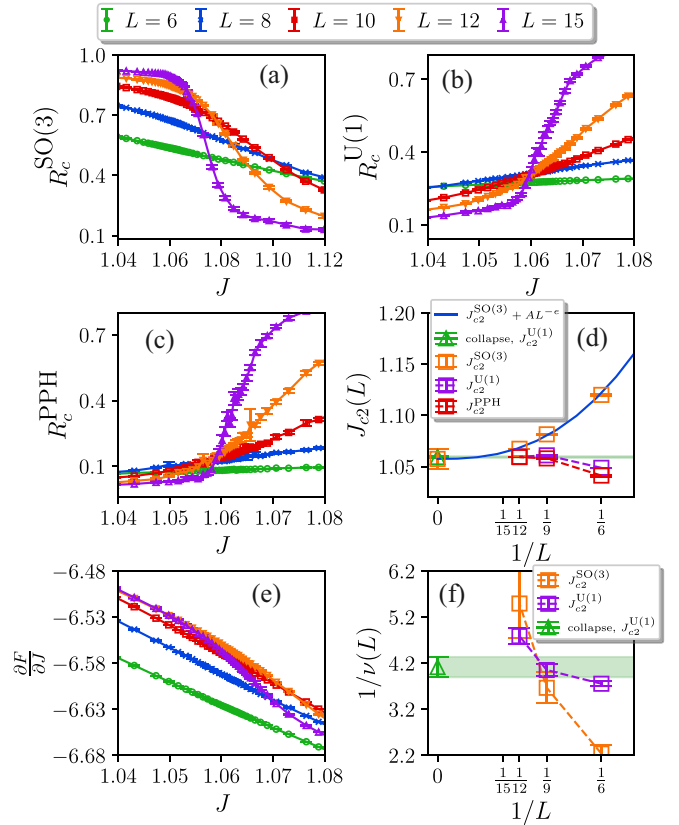

FIG. 6. (a) SO(3) correlation ratio $R_c^{SO(3)}$ as function of J in the vicinity of the SO(3)-U(1) transition for different fixed lattice sizes L. (b) Same as (a), but for the U(1) correlation ratio $R_c^{U(1)}$. (c) Same as (a), but for the PPH correlation ratio R_c^{PPH}. (d) Finite-size critical coupling $J_{c2}(L)$ as function of $1/L$ from crossing-point analysis of SO(3) correlation ratio (orange squares), U(1) correlation ratio (purple squares), and PPH correlation ratio (red squares). Blue solid curve indicates a power-law fit of $J_{c2}(L) = J_{c2} + aL^{-e}$ from SO(3) correlation ratio, yielding $J_{c2} = 1.057(10)$. Critical coupling J_{c2} from data-collapse analysis of U(1) correlation ratio is also shown for comparison (green triangle). All values for J_{c2} are consistent with each other, indicating a direct SO(3)-U(1) transition without an intermediate coexistence phase. (e) First derivative of free energy F as function of J, showing no discontinuity near J_{c2} within our accuracy. (f) Effective finite-size critical exponent $1/\nu(L)$ as function of $1/L$ from crossing-point analysis of SO(3) correlation ratio (orange squares) and U(1) correlation ratio (purple squares), in comparison with estimate for $1/\nu$ from data-collapse analysis of U(1) correlation ratio (green triangle).

Importantly, the finite-size critical couplings $J_{c2}(L)$ associated with the three different order parameters all scale towards a unique limiting value of $J_{c2} = 1.057(10)$ (orange triangle at $1/L = 0$). This indicates a direct transition at J_{c2} between the two different symmetry-broken states, without an intermediate coexistence phase. In Fig. 6(d), we present the first derivative of the free energy F as function of J in the vicinity of J_{c2}. Up to the largest system sizes considered ($L \leqslant 15$), no discontinuity in $\partial F/\partial J$ can be identified, in sharp contrast to the mean-field result [32]. This suggests a fluctuation-induced continuous or weakly first-order transition at J_{c2}. In order to characterize the associated quantum critical behavior,
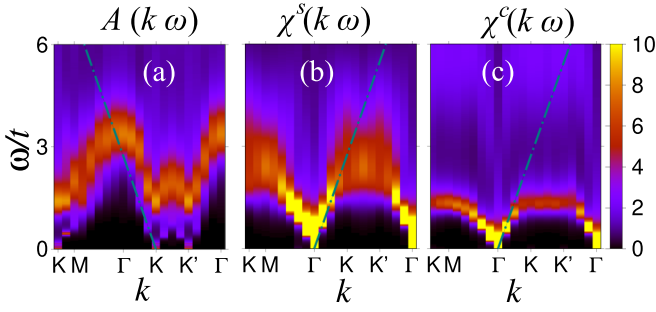
FIG. 7. Spectral functions in (a) single-particle, (b) particle-hole, and (c) particle-particle channels at the SO(3)-U(1) transition point for $J = 1.057 \approx J_{c2}$. Here, we show data for system size $L = 12$ and inverse temperature $\beta = 24$. Dash-dotted lines indicate the linear dispersions of the gapless excitations around the **K** (single-particle channel) and **Γ** (particle-hole and particle-particle channels) points in the Brillouin zone. The data support emergent Lorentz symmetry characterized by a single "velocity of light."

we attempt a scaling collapse of $R_c^{U(1)}(J, L)$ as function of $(J - J_{c2})L^{1/\nu}$. The resulting values of J_{c2} and $1/\nu$ are shown in Figs. 6(d) and 6(f), respectively (green triangles). We note that the value of J_{c2} from the data-collapse analysis is consistent with the extrapolation of the correlation-ratio crossing points [Fig. 6(d)]. For comparison, Fig. 6(f) also shows estimates for the correlation-length exponent $1/\nu$ from a crossing-point analysis analogous to Eq. (40), replacing $J_{c1} \rightarrow J_{c2}$ therein and choosing $c = 3$. Several remarks are in order: First, the autocorrelation time in the QMC simulations significantly increases near J_{c2}, as illustrated in Fig. 2(b). This restricts the available system sizes in the vicinity of J_{c2} to $L \leqslant 15$. Second, for the available system sizes, there is a significant drift in the estimates for $1/\nu$, suggesting the presence of sizable corrections to scaling. Third, we note that the finite-size values for $1/\nu(L)$ from the SO(3) and U(1) correlation ratios are consistent with each other within the numerical uncertainty, pointing towards a unique value for $1/\nu$ from the two different correlation functions. Fourth, if we assume a dynamical exponent $z = 1$, the estimates for $1/\nu$ are above the value $d + z$ expected for a first-order transition [39,50–53]. These results are again consistent with our interpretation of a fluctuation-induced continuous or weakly first-order order-to-order transition at J_{c2}. We refrain from estimating fermion and order-parameter anomalous dimensions, as the corresponding fitting processes in the scaling-collapse analysis involve an additional free parameter and are therefore even harder to control.

Spectral functions in different channels and at the critical point provide valuable insight on emergent symmetries. For instance, Lorentz symmetry imposes the constraint of a channel-independent velocity. In Fig. 7, we use the ALF [41] implementation of the stochastic maximum entropy methods [54] to compute the spectral functions in the single particle,

$$A_c(\boldsymbol{k}, \omega) = \pi \sum_{n, \lambda} |\langle n | \hat{\mathfrak{c}}_{\boldsymbol{k}, \lambda}^\dagger | 0 \rangle|^2 \delta(E_n - E_0 - \omega), \qquad (47)$$

particle-hole,

$$\chi^s(\boldsymbol{k}, \omega) = \pi \sum_{n, \lambda} |\langle n | \hat{\mathfrak{s}}_{\boldsymbol{k}, \lambda} | 0 \rangle|^2 \delta(E_n - E_0 - \omega), \qquad (48)$$

and particle-particle,

$$\chi^c(\boldsymbol{k}, \omega) = \pi \sum_n |\langle n | \hat{\Delta}_{\boldsymbol{k}}^\dagger | 0 \rangle|^2 \delta(E_n - E_0 - \omega), \qquad (49)$$

channels, where $|n\rangle$ and E_n, $n = 0, 1, 2, \dots$, correspond to the energy eigenstates and eigenvalues, respectively. Here, we consider $J \approx J_{c2} = 1.057(10)$. As apparent from Fig. 7, all quantities show a linear dispersion relation at low energy. The single-particle spectral function is gapless at the **K** and **K′** points in the Brillouin zone, while the particle-particle and particle-hole spectral functions are gapless at the **Γ** point. The gapless excitations in the particle-particle and particle-hole channels can be understood as collective modes associated with the SO(3) and U(1) order parameters, which characterize the neighboring long-range-ordered phases. Importantly, the velocity in all three aforementioned channels are comparable, such that the data support emergent Lorentz symmetry characterized by a single "velocity of light."

VI. FINITE-TEMPERATURE RESULTS

Further insight into the nature of the SO(3)-U(1) transition can be obtained by studying the finite-temperature properties above the potential quantum critical point. Since the interlayer-coherent insulating or s-wave superconducting state at $J > J_{c2}$ breaks U(1) charge and $\mathbb{Z}_2$ PPH symmetries only, we expect that the gapped phase extends to finite temperatures up to a critical temperature $T_c(J)$. By contrast, the SO(3)-spin-symmetry-broken state for $J < J_{c2}$, is expected to destabilize at arbitrary small temperatures as a consequence of the Mermin-Wagner theorem.

In order to investigate the finite-temperature properties, we compute the uniform susceptibilities [55]

$$\chi_{\text{uni}}^{\text{SO(3)}} = \frac{\beta}{L^2} (\langle \hat{\vec{S}} \cdot \hat{\vec{S}} \rangle - \langle \hat{\vec{S}} \rangle \cdot \langle \hat{\vec{S}} \rangle) \qquad (50)$$

measuring SO(3) spin fluctuations, with the total-spin operator $\hat{\vec{S}} = (\hat{S}^\alpha) = \sum_i \hat{c}_{i,\sigma,\lambda}^\dagger K_{\sigma\sigma'}^\alpha \hat{c}_{i,\sigma',\lambda}$, which generates SO(3) rotations, and

$$\chi_{\text{uni}}^{\text{U(1)}} = \frac{\beta}{L^2} (\langle \hat{\rho}\hat{\rho} \rangle - \langle \hat{\rho} \rangle \langle \hat{\rho} \rangle) \qquad (51)$$

measuring U(1) charge fluctuations, with the total-charge operator $\hat{\rho} = \sum_i \hat{c}_{i,\sigma,\lambda}^\dagger \hat{c}_{i,\sigma,\lambda}$, which generates U(1) rotations.

The results for the uniform susceptibilities as function of temperature are shown for three different values below, near, and above, respectively, the SO(3)-U(1) transition point in Fig. 8. For strong coupling $J > J_{c2}$ above the interlayer-coherent insulating or s-wave superconducting ground state, the SO(3) susceptibility $\chi_{\text{uni}}^{\text{SO(3)}}$ is strongly suppressed at low temperatures, in agreement with the expectation of an exponential decay, see Fig. 8(c). This reflects the gapped nature of the SO(3) spin spectral function in this phase. By contrast, the U(1) susceptibility $\chi_{\text{uni}}^{\text{U(1)}}$ approaches a finite value in the low-temperature limit, see Fig. 8(f), reflecting the low-energy spectral weight in the U(1) charge spectral function in
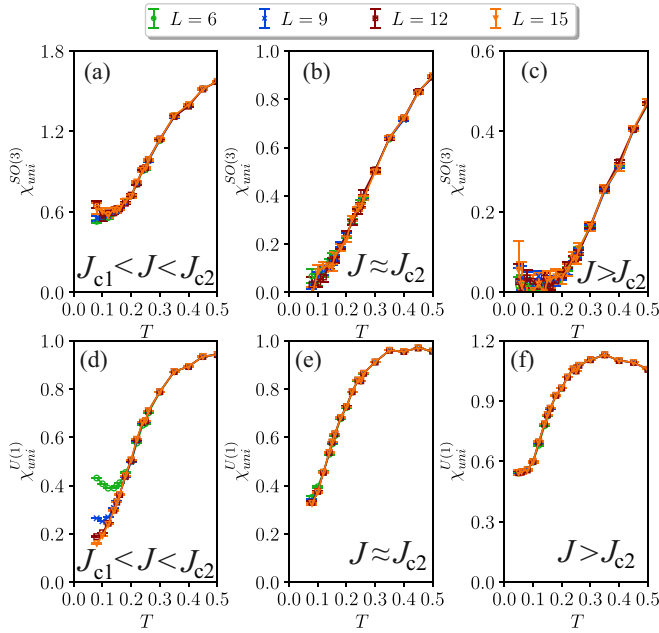
FIG. 8. (a) Uniform SO(3) susceptibility $\chi_{\text{uni}}^{\text{SO(3)}}$ as function of temperature for a representative fixed value of $J = 0.80$ below the SO(3)-U(1) transition point. (b) Same as (a), but for a value of $J = 1.06$ close to the SO(3)-U(1) transition point. (c) Same as (a), but for a value of $J = 1.30$ above the SO(3)-U(1) transition point. (d) Uniform SO(3) susceptibility $\chi_{\text{uni}}^{\text{U(1)}}$ as function of temperature for a representative fixed value of $J = 0.80$ below the SO(3)-U(1) transition point. (e) Same as (d), but for a value of $J = 1.06$ close to the SO(3)-U(1) transition point. (f) Same as (d), but for a value of $J = 1.30$ above the SO(3)-U(1) transition point.

this phase. For intermediate coupling $J_{c1} < J < J_{c2}$ above the SO(3)-spin-symmetry-broken ground state, the SO(3) susceptibility $\chi_{\text{uni}}^{\text{SO(3)}}$ approaches a finite value in the low-temperature limit [Fig. 8(a)], indicating the onset of short-range order in the SO(3) spin sector. The U(1) susceptibility $\chi_{\text{uni}}^{\text{U(1)}}$ is consistent with a linear behavior as function of temperature T at low T, reflecting the semimetallic behavior of the underlying SO(3) ground state [Fig. 8(d)]. At finite temperatures above a quantum critical point, we expect that the uniform susceptibilities scale with temperature as $\chi_{\text{uni}} \propto T^{2/z-1}$, where z corresponds to the dynamical critical exponent [55]. Assuming $z = 1$ leads to a linear-in-T behavior. In the vicinity of the SO(3)-U(1) transition point at J_{c2}, our data for both $\chi_{\text{uni}}^{\text{SO(3)}}$ and $\chi_{\text{uni}}^{\text{U(1)}}$ are indeed consistent with a linear-in-T dependence in the low-temperature limit, see Figs. 8(b) and 8(e). This again confirms our interpretation of a continuous or weakly first-order SO(3)-U(1) transition.

In order to characterize the finite-temperature phase boundary $T_c^{\text{U(1)}}(J)$, below which U(1) symmetry is spontaneously broken for $J > J_{c2}$, we also compute the momentum-resolved U(1) susceptibility

$$\chi_{\boldsymbol{k}}^{\text{U(1)}} = \int d\tau \, \mathcal{S}_{\text{U(1)}}(\boldsymbol{k}, \tau), \qquad (52)$$

where $\mathcal{S}_{\text{U(1)}}$ is the U(1) structure factor defined in Eq. (44). We expect the low-temperature phase at $T < T_c^{\text{U(1)}}(J)$ to be bounded by a Berezenskii-Kosterlitz-Thouless (BKT) transition [56–58], associated with the U(1)-charge-symmetry-

broken ground state at $J > J_{c2}$. The low-temperature phase is characterized by algebraic order that scales as $r^{-\eta}$ as function of distance r, with temperature-dependent anomalous dimension $\eta = \eta(T)$ for $T \leqslant T_c(J)$. Right at the BKT transition, the anomalous dimension becomes $\eta(T_c) = 0.25$. As a consequence, the BKT transition temperature can therefore be located by a crossing-point analysis of the rescaled U(1) susceptibility $L^{\eta-2}\chi_{\boldsymbol{k}=\Gamma}^{\text{U(1)}}$ with $\eta = 0.25$. Instead of scanning as function of temperature for fixed J, we may also use the coupling J as tuning parameter for the transition at fixed finite temperature T. This procedure turns out to be particularly useful in the vicinity of the SO(3)-U(1) quantum phase transition, in the vicinity of which the finite-temperature phase boundary in the plane spanned by J and T is very steep. The rescaled U(1) susceptibility $L^{\eta-2}\chi_{\boldsymbol{k}=\Gamma}^{\text{U(1)}}$ as function of J for different system sizes L and a representative fixed temperature is shown in Fig. 9(a). The corresponding crossing points $J_c^{\text{U(1)}}(T)$ are shown in the finite-temperature phase diagram for J near J_{c2} in Fig. 9(e). For larger values of J, the phase boundary in the plane spanned by J and T is rather flat, and it is more convenient to use the temperature as tuning parameter at fixed coupling J. The rescaled U(1) susceptibility $L^{\eta-2}\chi_{\boldsymbol{k}=\Gamma}^{\text{U(1)}}$ as function of T for different system sizes L and a representative fixed large value of J is shown in Fig. 9(b). The corresponding crossing points $T_c^{\text{U(1)}}(J)$ are shown in the finite-temperature phase diagram for large J well above J_{c2} in Fig. 9(f).

In the low-temperature phase for $T < T_c^{\text{U(1)}}$, the system spontaneously selects an s-wave superconducting or interlayer-coherent insulating state as ground state. This implies that $\mathbb{Z}_2$ PPH symmetry is broken in this phase as well. As a consequence, a lower bound for the critical temperature T_c^{PPH}, marking the melting of PPH order, is given by the U(1) critical temperature $T_c^{\text{U(1)}}$, i.e., $T_c^{\text{PPH}} \geqslant T_c^{\text{U(1)}}$. An interesting question is whether the two critical temperatures coincide or differ. The latter scenario would imply an intermediate vestigial phase for $T_c^{\text{U(1)}} < T < T_c^{\text{PPH}}$, in which PPH symmetry is spontaneously broken, but both U(1) global-charge and U(1) layer-charge symmetries remain intact. Such vestigial orders have previously been discussed in a variety of two-dimensional models [37–39]. In order to characterize the melting of PPH order, we measure the PPH susceptibility

$$\chi_{\boldsymbol{k}}^{\text{PPH}} = \int d\tau \, \mathcal{S}_{\text{PPH}}(\boldsymbol{k}, \tau), \qquad (53)$$

where $\mathcal{S}_{\text{PPH}}$ is the PPH structure factor defined analogously to Eq. (44), using the parity operator $\hat{P}_i$ instead of the interlayer coherence operator $\hat{n}_i$. From the symmetry of the order parameter, we expect the PPH transition, if continuous, to fall into the 2D Ising universality class. In Fig. 9(c), we therefore show the rescaled PPH susceptibility $L^{\eta-2}\chi_{\boldsymbol{k}=\Gamma}^{\text{U(1)}}$ as function of J for different system sizes L and a representative fixed temperature [same temperature as those of the U(1) susceptibility shown in Fig. 9(a)], using the Ising exponent $\eta = 0.25$. Similarly, we show in Fig. 9(d) the rescaled PPH susceptibility as function of T for different system sizes L and a representative fixed large value of J [same coupling as those of the U(1) susceptibility shown in Fig. 9(b)] using $\eta = 0.25$. While the data clearly indicate the PPH order at sufficiently large J and low
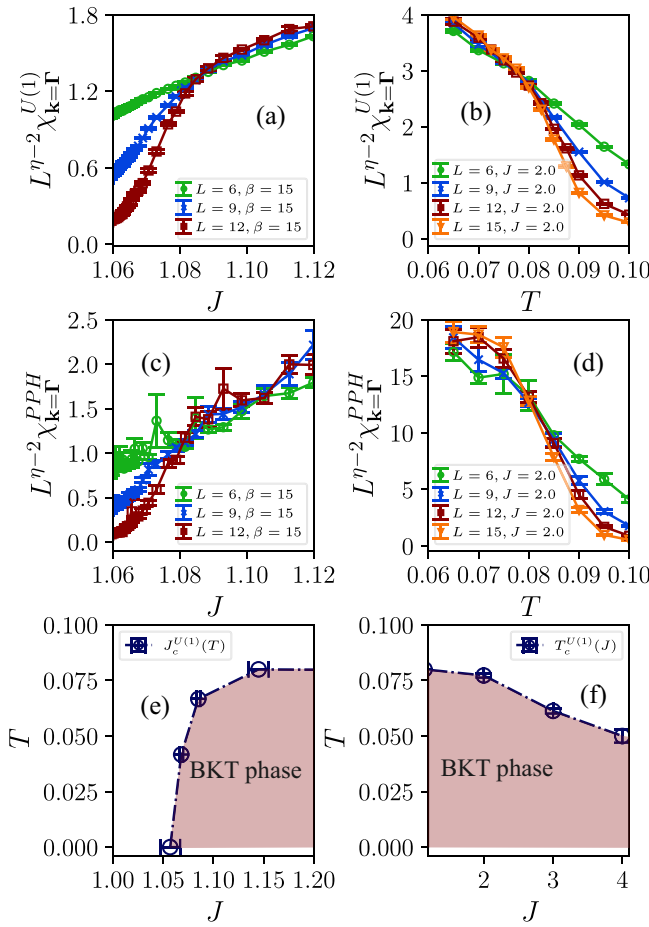
FIG. 9. (a) Rescaled U(1) susceptibility $L^{\eta-2}\chi_{\mathbf{k}=\Gamma}^{U(1)}$ for $\eta = 0.25$ as function of coupling J for different system sizes L and a representative fixed inverse temperature $\beta = 15$. The crossing point indicates the phase boundary $J_c^{U(1)}(T)$ at finite temperature $T = 1/\beta$. (b) Rescaled U(1) susceptibility $L^{\eta-2}\chi_{\mathbf{k}=\Gamma}^{U(1)}$ for $\eta = 0.25$ as function of temperature T for different system sizes L and a representative large value of the coupling $J = 2$ well above the SO(3)-U(1) transition. The crossing point indicates the finite-temperature phase boundary $T_c^{U(1)}(J)$. (c)(d) Same as (a) and (b), but for the rescaled PPH susceptibility $L^{\eta-2}\chi_{\mathbf{k}=\Gamma}^{PPH}$. (e) Finite-temperature phase diagram in the vicinity of the SO(3)-U(1) transition from crossings of rescaled U(1) susceptibility as function of J. Red region refers to phase characterized by algebraic order in the U(1)-charge sector ("BKT phase"). (f) Same as (c), but at large coupling J well above the SO(3)-U(1) transition from crossings of rescaled U(1) susceptibility as function of T.

T, they are too noisy to clearly identify whether the critical temperature T_c^{PPH} lies above or right at $T_c^{U(1)}$. This is also due to the fact that vestigial orders are typically realized in only small temperature windows above the corresponding primary orders [37–39]. The presence of a tiny vestigial phase above $T_c^{U(1)}$ can therefore at present not be excluded from our data. Exploring this possibility deserves further investigation.

VII. CONCLUSIONS

In this paper, we have characterized, by means of large-scale determinant QMC simulations, the metallic and

deconfined quantum phase transitions recently discovered in a bilayer honeycomb model with an SO(3)-symmetric spin-density interaction in terms of their quantum critical and finite-temperature properties. In comparison with our initial exploratory study of this model [32], we have employed a Hermitian Trotter decomposition, which significantly improves convergence properties with respect to the limit of small Trotter time steps. Furthermore, we have employed a microscopic implementation that preserves the model's partial particle-hole symmetry explicitly, maintaining the degeneracy of the interlayer-coherent insulating and s-wave superconducting ground states in the fully gapped phase stabilized at strong coupling already on finite lattice sizes.

These advances have lead to improved estimates for the critical exponents characterizing the Gross-Neveu-SO(3) quantum critical point at J_{c1}. From the data-collapse analysis, we have obtained $1/\nu = 0.86(8)$ for the correlation-length exponent, $\eta_\phi = 0.73(2)$ for the order-parameter anomalous dimension, and $\eta_\psi = 0.078(8)$ for the fermion anomalous dimensions. These results are consistent with earlier field-theoretical estimates [33] within the systematics uncertainties of both the numerical and field-theoretical approaches.

We have also provided a further characterization of the putative deconfined metallic quantum critical point at J_{c2}. In particular, the spectral functions in the single-particle, particle-hole, and particle-particle channel indicate gapless excitations with a unique "velocity of light," supporting the emergence of Lorentz symmetry at J_{c2}. We have also computed the finite-temperature phase diagram of the model and show that the boundary of the low-temperature phase vanishes continuously upon approaching J_{c2}, in agreement with the expectation for a continuous or weak first-order transition.

Our microscopic model features an explicit SO(3) × U(1) × $U_L(1)$ × $\mathbb{Z}_2$ symmetry in the spin, total-charge, layer-charge, and partial-particle-hole sectors. For the future, it would be interesting to investigate the possibility of an emergent higher symmetry at the SO(3)-U(1) transition. To this end, the decay of dynamical correlation functions of higher-symmetry generators should be studied. This could help to develop a field-theoretical understanding of the putative deconfined metallic transition, e.g., via a Wess-Zumino-Witten theory coupled to fermionic degrees of freedom.

Furthermore, it would be interesting to study the effects of explicit symmetry breaking, e.g., in the SO(3) spin sector. The Gross-Neveu-SO(3) transition at J_{c1} is expected to become a multicritical point featuring emergent SO(3) symmetry within the enlarged parameter space, and the SO(3)-spin-ordered semimetal phase at intermediate coupling $J_{c1} < J < J_{c2}$ is destabilized in favor of a SO(2)- or $\mathbb{Z}_2$-spin-ordered phase by the symmetry-breaking perturbations [59]. Since the U(1)-ordered phase at strong coupling $J > J_{c2}$ is gapped, one might expect that it is stable upon adding small symmetry-breaking perturbations in the spin sector. If that is correct, it would be interesting to study the nature of the transition between the SO(2)- or $\mathbb{Z}_2$-spin-ordered phases at intermediate coupling and the U(1)-ordered phase at strong coupling. This should

be expected to also lead to further insights into the nature of the putative deconfined metallic quantum critical point at J_{c2}.

A recent field-theoretical analysis [60] proposed the existence of another quantum critical point in a new universality class, which may be reached within the parameter space of our model by adding to the Hamiltonian an interaction of the form

$$\hat{H}_{J'} = -J' \sum_{i,\alpha<\beta} \left(\hat{c}_{i,\sigma,\lambda}^\dagger Q_{\sigma\sigma'}^{\alpha\beta} \hat{c}_{i,\sigma',\lambda} \right)^2, \tag{54}$$

with the real 3×3 matrices $Q^{\alpha\beta} = \frac{1}{2}\{K^\alpha, K^\beta\} - \frac{2}{3}\delta^{\alpha\beta}$. It would be interesting to investigate this conjecture numerically. As the vertex matrix associated with the above interaction is real, the model can be simulated using QMC simulations without a fermion sign problem for positive values of J'.

[1] M. A. Metlitski and S. Sachdev, Quantum phase transitions of metals in two spatial dimensions. I. Ising-nematic order, Phys. Rev. B **82**, 075127 (2010).

[2] M. A. Metlitski and S. Sachdev, Quantum phase transitions of metals in two spatial dimensions. II. Spin density wave order, Phys. Rev. B **82**, 075128 (2010).

[3] S. Sur and S.-S. Lee, Anisotropic non-Fermi liquids, Phys. Rev. B **94**, 195135 (2016).

[4] A. Schlief, P. Lunts, and S.-S. Lee, Exact critical exponents for the antiferromagnetic quantum critical metal in two dimensions, Phys. Rev. X **7**, 021010 (2017).

[5] S.-S. Lee, Recent developments in non-Fermi liquid theory, Annu. Rev. Condens. Matter Phys. **9**, 227 (2018).

[6] E. Berg, S. Lederer, Y. Schattner, and S. Trebst, Monte Carlo studies of quantum critical metals, Annu. Rev. Condens. Matter Phys. **10**, 63 (2019).

[7] A. Klein, A. V. Chubukov, Y. Schattner, and E. Berg, Normal state properties of quantum critical metals at finite temperature, Phys. Rev. X **10**, 031053 (2020).

[8] I. Esterlis, H. Guo, A. A. Patel, and S. Sachdev, Large-*N* theory of critical Fermi surfaces, Phys. Rev. B **103**, 235129 (2021).

[9] H. Guo, A. A. Patel, I. Esterlis, and S. Sachdev, Large-*N* theory of critical Fermi surfaces. II. Conductivity, Phys. Rev. B **106**, 115151 (2022).

[10] Z. H. Liu, B. Frank, L. Janssen, M. Vojta, and F. F. Assaad, Magnetic quantum phase transition in a metallic Kondo heterostructure, Phys. Rev. B **107**, 165104 (2023).

[11] B. Frank, Z. H. Liu, F. F. Assaad, M. Vojta, and L. Janssen, Marginal Fermi liquid at magnetic quantum criticality from dimensional confinement, Phys. Rev. B **108**, L100405 (2023).

[12] M. Vojta, Frustration and quantum criticality, Rep. Prog. Phys. **81**, 064501 (2018).

[13] T. Senthil, L. Balents, S. Sachdev, A. Vishwanath, and M. P. A. Fisher, Quantum criticality beyond the Landau-Ginzburg-Wilson paradigm, Phys. Rev. B **70**, 144407 (2004).

[14] A. B. Kuklov, M. Matsumoto, N. V. Prokof'ev, B. V. Svistunov, and M. Troyer, Deconfined criticality: Generic first-order transition in the SU(2) symmetry case, Phys. Rev. Lett. **101**, 050405 (2008).

[15] R. K. Kaul, R. G. Melko, and A. W. Sandvik, Bridging lattice-scale physics and continuum field theory with quantum Monte Carlo simulations, Annu. Rev. Condens. Matter Phys. **4**, 179 (2013).

[16] A. Nahum, J. T. Chalker, P. Serna, M. Ortuño, and A. M. Somoza, Deconfined quantum criticality, scaling violations, and classical loop models, Phys. Rev. X **5**, 041048 (2015).

[17] H. Shao, W. Guo, and A. W. Sandvik, Quantum criticality with two length scales, Science **352**, 213 (2016).

[18] B. Zhao, J. Takahashi, and A. W. Sandvik, Multicritical deconfined quantum criticality and Lifshitz point of a helical valence-bond phase, Phys. Rev. Lett. **125**, 257204 (2020).

[19] Y. Cui, L. Liu, H. Lin, K.-H. Wu, W. Hong, X. Liu, C. Li, Z. Hu, N. Xi, S. Li *et al.*, Proximate deconfined quantum critical point in $SrCu_2(BO_3)_2$, Science **380**, 1179 (2023).

[20] J. Zhao, Y.-C. Wang, Z. Yan, M. Cheng, and Z. Y. Meng, Scaling of entanglement entropy at deconfined quantum criticality, Phys. Rev. Lett. **128**, 010601 (2022).

[21] M. Song, J. Zhao, M .Cheng, C. Xu, M. M. Scherer, L. Janssen, and Z. Y. Meng, Deconfined quantum criticality lost, arXiv:2307.02547

[22] Z. Deng, L. Liu, W. Guo, and H. qing Lin, Diagnosing $SO(5)$ symmetry and first-order transition in the $J - Q_3$ model via entanglement entropy, arXiv:2401.12838.

[23] J. D'Emidio and A. W. Sandvik, Entanglement entropy and deconfined criticality: Emergent SO(5) symmetry and proper lattice bipartition, arXiv:2401.14396.

[24] T. Senthil, Deconfined quantum critical points: A review, arXiv:2306.12638.

[25] S. V. Isakov, R. G. Melko, and M. B. Hastings, Universal signatures of fractionalized quantum critical points, Science **335**, 193 (2012).

[26] M. Schuler, S. Whitsitt, L.-P. Henry, S. Sachdev, and A. M. Läuchli, Universal signatures of quantum critical points from finite-size torus spectra: A window into the operator content of higher-dimensional conformal field theories, Phys. Rev. Lett. **117**, 210401 (2016).

[27] S. Gazit, F. F. Assaad, S. Sachdev, A. Vishwanath, and C. Wang, Confinement transition of $\mathbb{Z}_2$ gauge theories coupled to massless fermions: Emergent quantum chromodynamics and

SO(5) symmetry, Proc. Natl. Acad. Sci. USA **115**, E6987 (2018).

[28] L. Janssen and Y.-C. He, Critical behavior of the QED$_3$-Gross-Neveu model: Duality and deconfined criticality, Phys. Rev. B **96**, 205113 (2017).

[29] L. Janssen, W. Wang, M. M. Scherer, Z. Y. Meng, and X. Y. Xu, Confinement transition in the QED$_3$-Gross-Neveu-XY universality class, Phys. Rev. B **101**, 235118 (2020).

[30] U. F. P. Seifert, X.-Y. Dong, S. Chulliparambil, M. Vojta, H.-H. Tu, and L. Janssen, Fractionalized fermionic quantum criticality in spin-orbital Mott insulators, Phys. Rev. Lett. **125**, 257202 (2020).

[31] U. Borla, S. Gazit, and S. Moroz, In pursuit of deconfined quantum criticality in Ising gauge theory entangled with single-component fermions, arXiv:2402.00933.

[32] Z. H. Liu, M. Vojta, F. F. Assaad, and L. Janssen, Metallic and deconfined quantum criticality in Dirac systems, Phys. Rev. Lett. **128**, 087201 (2022).

[33] S. Ray, B. Ihrig, D. Kruti, J. A. Gracey, M. M. Scherer, and L. Janssen, Fractionalized quantum criticality in spin-orbital liquids from field theory beyond the leading order, Phys. Rev. B **103**, 155160 (2021).

[34] B. Mondal, V. B. Shenoy, and S. Bhattacharjee, Emergent SU(8) Dirac semimetal and novel proximate phases of spin-orbit coupled fermions on a honeycomb lattice, arXiv:2304.07223.

[35] Note that the "fully gapped state" exhibits a finite gap in the single-particle spectrum while still retaining a gapless Goldstone excitation in the two-particle spectrum, associated with the spontaneously broken U(1) symmetry.

[36] L. Zou and D. Chowdhury, Deconfined metallic quantum criticality: A $U(2)$ gauge-theoretic approach, Phys. Rev. Res. **2**, 023344 (2020).

[37] B. V. Svistunov, E. S. Babaev, and N. V. Prokof'ev, *Superfluid States of Matter* (CRC Press, Boca Raton, FL, 2015).

[38] R. M. Fernandes, P. P. Orth, and J. Schmalian, Intertwined vestigial order in quantum materials: Nematicity and beyond, Annu. Rev. Condens. Matter Phys. **10**, 133 (2019).

[39] N. Francini and L. Janssen, Spin vestigial orders in extended Heisenberg-Kitaev models near hidden SU(2) points: Application to Na$_2$Co$_2$TeO$_6$, Phys. Rev. B **109**, 075104 (2024).

[40] S. Chulliparambil, U. F. P. Seifert, M. Vojta, L. Janssen, and H.-H. Tu, Microscopic models for Kitaev's sixteen-fold way of anyon theories, Phys. Rev. B **102**, 201111(R) (2020).

[41] F. F. Assaad, M. Bercx, F. Goth, A. Götz, J. S. Hofmann, E. Huffman, Z. Liu, F. Parisen Toldin, J. S. E. Portela, and J. Schwab, The ALF (Algorithms for Lattice Fermions) project release 2.0. Documentation for the auxiliary-field quantum Monte Carlo code, SciPost Phys. Codebases **1** (2022).

[42] R. Blankenbecler, D. J. Scalapino, and R. L. Sugar, Monte Carlo calculations of coupled boson-fermion systems. I, Phys. Rev. D **24**, 2278 (1981).

[43] S. R. White, D. J. Scalapino, R. L. Sugar, E. Y. Loh, J. E. Gubernatis, and R. T. Scalettar, Numerical study of the two-dimensional Hubbard model, Phys. Rev. B **40**, 506 (1989).

[44] G. Sugiyama and S. Koonin, Auxiliary field Monte-Carlo for quantum many-body ground states, Ann. Phys. (NY) **168**, 1 (1986).

[45] S. Sorella, S. Baroni, R. Car, and M. Parrinello, A novel technique for the simulation of interacting fermion systems, Europhys. Lett. **8**, 663 (1989).

[46] F. F. Assaad, M. Imada, and D. J. Scalapino, Charge and spin structures of a $d_{x^2-y^2}$ superconductor in the proximity of an antiferromagnetic Mott insulator, Phys. Rev. B **56**, 15001 (1997).

[47] R. K. Kaul, Spin nematics, valence-bond solids, and spin liquids in SO(N) quantum spin models on the triangular lattice, Phys. Rev. Lett. **115**, 157202 (2015).

[48] M. Campostrini, A. Pelissetto, and E. Vicari, Finite-size scaling at quantum transitions, Phys. Rev. B **89**, 094516 (2014).

[49] F. P. Toldin, M. Hohenadler, F. F. Assaad, and I. F. Herbut, Fermionic quantum criticality in honeycomb and π-flux Hubbard models: Finite-size scaling of renormalization-group-invariant observables from quantum Monte Carlo, Phys. Rev. B **91**, 165108 (2015).

[50] B. Nienhuis and M. Nauenberg, First-order phase transitions in renormalization-group theory, Phys. Rev. Lett. **35**, 477 (1975).

[51] M. E. Fisher and A. N. Berker, Scaling for first-order phase transitions in thermodynamic and finite systems, Phys. Rev. B **26**, 2507 (1982).

[52] K. Binder, Theory of first-order phase transitions, Rep. Prog. Phys. **50**, 783 (1987).

[53] M. Mueller, W. Janke, and D. A. Johnston, Nonstandard finite-size scaling at first-order phase transitions, Phys. Rev. Lett. **112**, 200601 (2014).

[54] K. S. D. Beach, Identifying the maximum entropy method as a special limit of stochastic analytic continuation, arXiv:cond-mat/0403055.

[55] M. Hohenadler, Y. Liu, T. Sato, Z. Wang, W. Guo, and F. F. Assaad, Thermodynamic and dynamical signatures of a quantum spin Hall insulator to superconductor transition, Phys. Rev. B **106**, 024509 (2022).

[56] V. L. Berezinskii, Destruction of long-range order in one-dimensional and two-dimensional systems having a continuous symmetry group I. Classical systems, Sov. Phys. JETP **32**, 493 (1971).

[57] J. M. Kosterlitz and D. J. Thouless, Ordering, metastability and phase transitions in two-dimensional systems, J. Phys. C: Solid State Phys. **6**, 1181 (1973).

[58] J. Kosterlitz, The critical properties of the two-dimensional XY model, J. Phys. C: Solid State Phys. **7**, 1046 (1974).

[59] M. Fornoville, Fractionalized fermionic quantum criticality in Kitaev spin-orbital models, Master's thesis, TU Dresden, 2024.

[60] S. Ray, Unconventional Gross-Neveu quantum criticality: Interaction-induced SO(3)-biadjoint insulator and emergent SU(3) symmetry, Phys. Rev. B **109**, 165137 (2024).